

Article

1-D Modeling of Two Phase Flow Process in Concentric Annular Heat Pipe and Experimental Investigation

Ji-Su Lee, Jae-Hyun Ahn, Heui-Il Chae, Hi-Chan Lee and Seok-Ho Rhi * 

School of Mechanical Engineering, Chungbuk National University, Cheongju 28644, Korea; dlwlt1515@chungbuk.ac.kr (J.-S.L.); ajh4421@chungbuk.ac.kr (J.-H.A.); chaeheuiil@gmail.com (H.-I.C.); gmlcks369@naver.com (H.-C.L.)

* Correspondence: rhi@chungbuk.ac.kr

Abstract: As the heat dissipation of smart devices increases, cutting-edge cooling solutions are becoming increasingly important. The heat pipe is an efficient device that boosts heat transfer and is recommended to reduce thermal management power. In this study, a concentric annular heat pipe (CAHP) with distilled water as a working fluid is proposed to enhance heat transfer, and experiments and one-dimensional analysis were carried out to predict thermal characteristics and evaluate performance. The CAHP was 90 mm in length, 62 mm in inner diameter, 70 mm in outer diameter, and 0.4 mm in thickness. At the outer surface of the internal CAHP, a two-layer screen mesh wick (500 mesh, Stainless Steel 304) that is 0.34 mm in layer thickness was installed. A ceramic heater (20 mm × 20 mm) was attached to the middle of the outer surface, and the hollow region with 48 fins was cooled by an electric fan. The experiment was carried out with variations in the heat load, the filling ratio of the working fluid, the pitch angle, the roll angle, and the airflow speed, and the one-dimensional analysis was modeled by AMESIM. The experimental results showed that the best thermal resistance of the CAHP was 3.74 °C/W with a supplied heat of 20 W, a pitch angle of -15° , and a V_{air} of 3 m/s. In addition, the CAHP's 1-D simulation model using AMESIM was verified through the experimental results. However, although the modeling results according to the inclination angle could not be reflected due to the difficulty of implementing multiple orientation structures in the one-dimensional simulation model, the simulation results were found to be almost consistent with the experimental results. Case studies were conducted to understand the various characteristics of the CAHP using the model, and the optimal volume fraction, the porosity, and the number of layers of the wicks were determined to be 10, 0.345, and 2, respectively.

Keywords: concentric annular heat pipe; one-dimensional analysis; AMESIM; heat sink; cooling; electronics



Citation: Lee, J.-S.; Ahn, J.-H.; Chae, H.-I.; Lee, H.-C.; Rhi, S.-H. 1-D Modeling of Two Phase Flow Process in Concentric Annular Heat Pipe and Experimental Investigation. *Processes* **2022**, *10*, 493. <https://doi.org/10.3390/pr10030493>

Academic Editors: Paolo Blecich and Tomislav Mrakovčić

Received: 7 January 2022

Accepted: 8 February 2022

Published: 1 March 2022

Publisher's Note: MDPI stays neutral with regard to jurisdictional claims in published maps and institutional affiliations.



Copyright: © 2022 by the authors. Licensee MDPI, Basel, Switzerland. This article is an open access article distributed under the terms and conditions of the Creative Commons Attribution (CC BY) license (<https://creativecommons.org/licenses/by/4.0/>).

1. Introduction

As the heat dissipation of smart devices for battery electric vehicles increases, the IIoT (Industrial Internet of Things), the cloud system, and other cutting-edge cooling solutions for electronic devices are becoming increasingly important [1–3]. In this research, a new idea was attempted to overcome the difficulty of water-cooled structures. In general, a power semiconductor of an electric vehicle attempts to cool through a cooling channel composed of multiple fins, but a large flow rate in the refrigerant and a large thermal contact surface must be ensured in order to effectively achieve cooling that contacts only part of the heating source. However, the annular heat pipe developed in this study, by installing a cooling channel in the annular center space, has the advantage of securing space so that it can directly contact the heat, so its applicability is excellent. In addition, since its operating characteristics have been identified in this study, continuous research is expected to be conducted in the future to determine its value as a future electric vehicle or semiconductor cooling device [4–7]. Elnagar et al. [8] analyzed recent trends by investigating application

cases of heat pipes for CPU cooling. Although the number of applications of heat pipes has been steadily increasing, it has been confirmed that the demand for thin-film heat pipes has also increased due to the recent reduction of core sizes in computers and tablets.

Smakulski et al. [9] reviewed various cooling methods, such as the use of porous materials, microchannels, and spray cooling. They reported that the heat from the hot spots of future high-power components can reach heat fluxes of up to 500 W/cm^3 , and this supports the need for new ideas about heat removal and thermal management systems.

A heat pipe is a highly efficient thermal management device that enables fast heat transfer without consuming power by using a two-phase flow of a working fluid, and for this reason, applying a heat pipe to high-performance smart devices is recommended to reduce thermal management power [10]. As illustrated in Figure 1a, the conventional heat pipe uses the phase change of a working fluid to transfer heat remarkably quickly from the heat source to the heat sink. Due to this, heat pipes are classified as highly efficient devices. According to thermodynamics, the fluid evaporates at a temperature lower than the boiling temperature when the pressure is lower than 1 atm. Using this phenomenon, the working fluid is injected into a vacuum container of the heat pipe to improve the performance of the phase change. The heat pipe generally consists of three regions: the evaporator section, the adiabatic section, and the condenser section. The working fluid evaporates, and the vapor with heat then moves to the condenser section because of the pressure difference. The vapor is condensed at the condenser and recirculated by the capillary force of gravity. There are many different types of heat pipes, but they are mainly two classifications: thermosyphons and heat pipes, which are classified as having a wick structure or not. The thermosyphon recirculates a working fluid using gravity, but a heat pipe uses capillary force with its wick structure. On the other hand, classifying heat pipes by their use and shape, there are many different types: a constant conductance heat pipe (CCHP), a loop heat pipe (LHP), an oscillating heat pipe (OHP), a variable conductance heat pipe (VCHP), a flexible heat pipe, and so on. Furthermore, a heat pipe can operate in a very wide range of temperatures, from -271 to $2200 \text{ }^\circ\text{C}$, according to the various working fluids [4,5,10,11].

Faghri et al. [12] attempted a comparison by theoretically modeling a conventional thermosyphon and an annular thermosyphon. They conducted a characteristic comparison of flooding limits. Faghri and Thomas [13,14] carried out experiments on a concentric annular heat pipe (CAHP) with a wick structure and conducted a simple analysis to predict its capillary limit. They emphasized that annular heat pipes have the very advantageous aspect of greatly expanding the heat transfer surface area in the condenser.

Boo et al. [15] investigated the performance and thermal characteristics of a copper annular heat pipe with a screen mesh wick located on the surface and a bridge wick. Their results showed that the minimum thermal resistance of the annular heat pipe was $0.03 \text{ }^\circ\text{C/W}$.

Yan et al. [16] studied an annular sodium heat pipe designed for furnaces. They reported that an annular sodium heat pipe operated from 500 to $1200 \text{ }^\circ\text{C}$. Choi et al. [17] constructed an annular heat pipe with naphthalene as a working fluid and applied it to the sintering process using the internal space of a concentric annular heat pipe. Kammuang-lue et al. [18] studied three concentric annular thermosyphons and found that annular thermosyphons (ATs) outperform traditional thermosyphons. Mustafar et al. [19] studied an annular heat pipe with stainless steel under various experimental conditions—an angle of 0 to 90° and a filling ratio of working fluid from 11% to 43% —and found that the optimal condition of an annular heat pipe is when the internal filling ratio is 11% .

Song et al. [20] experimented with a concentric annular heat pipe heat sink (CAHPHS) in order to study its thermal performance and characteristics. The shape of a CAHPHS has a significant advantage in enhancing the heat transfer area for cooling compared to conventional heat pipes. They experimentally studied the CAHPHS with various conditions—a diameter ratio of 1.1 or 1.3 , a volume fraction of $10\text{--}70\%$, and a supplied heat of $10\text{--}50 \text{ W}$. Their results showed that the optimal filling ratio of a CAHPHS is 10% , and the behavior of the internal working fluid showed 3-D flow characteristics. Song et al. [21]

analyzed a concentric annular heat pipe (CAHP) using CFD. They conducted 2-D and 3-D analyses, and the simulation results were validated by the experimental results.

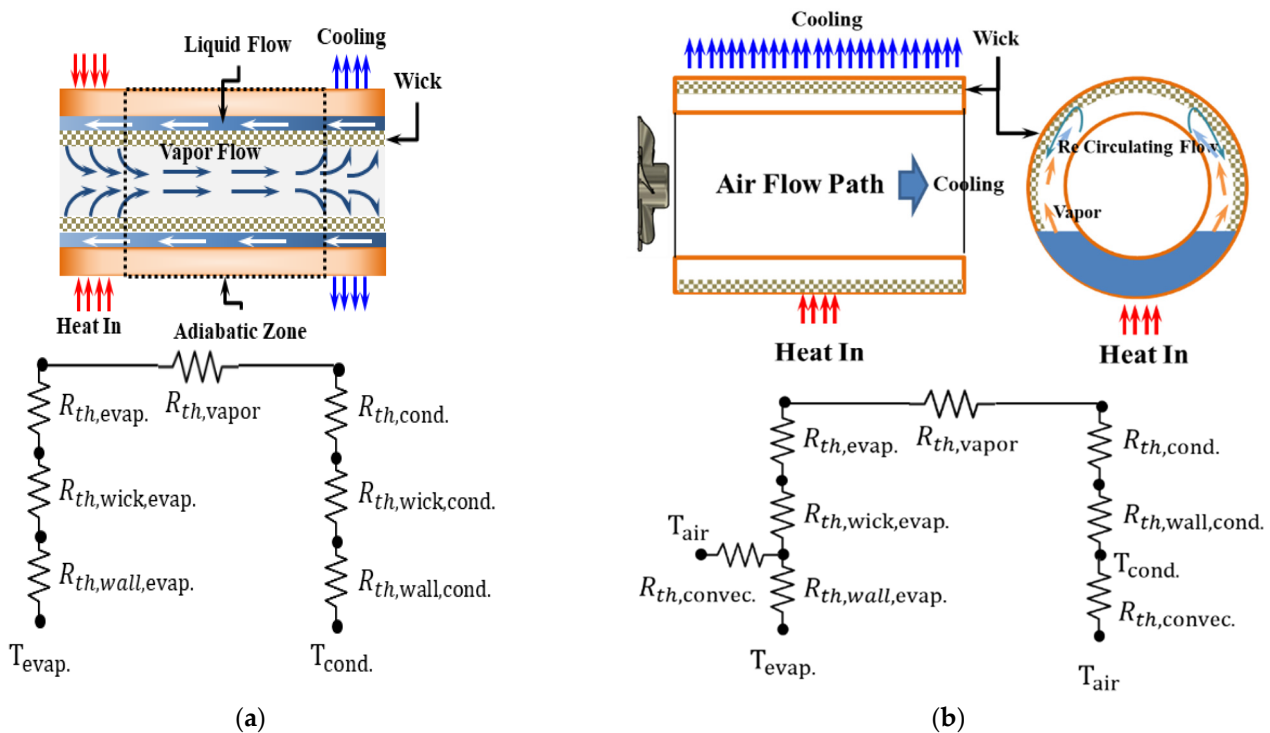


Figure 1. Thermal Resistance Network of a Conventional Heat Pipe and a CAHP. (a) Thermal Resistance Network of a Conventional Heat Pipe. (b) Thermal Resistance Network of a CAHP.

Czajkowski et al. [22] studied a special type of oscillating heat pipe and a flower shape by changing the rotating velocity, the heat load, and the filling ratio. Their results show that the flow of the working fluid was boosted when applying a higher temperature amplitude in the rotary system.

Blasiak et al. [23] studied a pulsating heat pipe using 2-D multiphase simulation. For this simulation, the VOF (volume of fluid) model was adopted, and the analysis was carried out with various mass transfer models between phases. Their study showed that the 2-D multi-phase modeling results had a relative error within a range of about 10% compared to the results obtained by the experiment.

Khalili et al. [24] investigated the thermal performance of a new type of sintered heat pipe, i.e., a partially sintered heat pipe. They used distilled water and acetone as working fluids to examine the effects of the charge ratio, direction, and heat input. In addition, conditions under which dry-out occurs were also suggested. As a result, performance was compared according to the charged amounts of 10–45% for the two working fluids, and the optimum charged ratio was about 20%. The thermal resistance of the water-filled heat pipe was lower than that of the acetone-filled heat pipe in vertical and horizontal modes.

Alves et al. [25] experimentally investigated the thermal performance of a heat pipe and a thermosyphon. They developed a heat pipe to cool the heating part of the thermoelectric module and evaluated the performance of the thermosyphon and the groove or sintering wick heat pipes at vertical or horizontal positions.

Kapekov [26] conducted a one-dimension analysis of a conventional heat pipe using AMESIM and compared the results with the experimental results. Very similar results were obtained.

Liu et al. [27] performed dynamic modeling for an electric vehicle battery cooling system using a heat pipe. Their model was calculated by segmenting the thermal resistance to improve the accuracy of the calculation. In addition, it was proven that the subdivided

calculation result of the resistance has much higher accuracy. In addition, Lee [28] presented a lumped capacity model based on a heat pipe's one-dimensional thermal resistance network and conducted a study to analyze factors such as porosity, boiling, and the condensation heat transfer coefficient, variables for resistance. Shafieian et al. [29] reported various studies on the modeling of heat pipes used in solar vacuum tubes. Most of their reported cases were lumped capacity models by one-dimensional thermal resistance networks, and some two-dimensional CFD models were reported. Ciacci [30] and Hu et al. [31] performed thermal modeling of electric vehicle thermal management systems and micro-reactors. In the process of performing a one-dimensional model, a multi-physics model through AMESIM and two-dimensional CFD were presented. Thus, they showed examples of complex calculations incorporating different physical theories of the entire system, as opposed to local modeling. In addition, Yoo [32] also showed an example of a multi-physics simulation that performs complex modeling when a heat pipe is connected as a part of an applied system.

Dong et al. [33] and Tao [34] reported one-dimensional modeling using AMESIM. Dong et al. attempted to develop a temperature control system for an air electronic equipment liquid cooling system through model simulation. In addition, they simplified the system and established a numerical calculation model for the heat transfer of major components. Tao [34] also used a one-dimensional method to analyze the battery cooling system of a hybrid electrical vehicle. He maximized efficiency in the system design through the use of AMESIM by linking Simulink to the entire system configuration. The thermal management system manufactured through the optimum design using AMESIM showed a performance improvement of 50% compared to the performance of a typical vapor compression cooling system.

Several heat pipes [35–39] have been subject to numerical analysis. One of the best-known methods is the lumped capacity model, which sees the wicks of heat pipes and various components as one conductive medium and simplifies them by configuring a thermal resistance network. Another analytical technique is computational fluid dynamics (CFD) modeling using a volume of fluid (VOF) model that involves several assumptions locally. CFD modeling takes time to calculate, so most models are two-dimensional simulations [35–39]. Some researchers presented three-dimensionally modeled internal flows to show various types of internal flows [21]. Additionally, few researchers [26,30,33,34] showed that the one-dimensional AMESIM model to be performed in this study has the advantage of modeling based on the multi-physics theory, where all constituent factors are subdivided into one resistance element, unlike the existing simplified lumped model. However, it is difficult to connect each component one-dimensionally, requiring a complete understanding of the two-phase flow inside the heat pipe. In this study, since the theoretical principle of AMESIM is composed of libraries—one of its advantages—it is effectively connected and can implement a two-phase flow inside the CAHP, simulate it, and determine the optimal operating characteristics.

This paper intends to present the results of experiments and simulations on heat sinks using a CAHP, which have not been found in existing research. Unlike typical heat pipes, the CAHP presented in this study has an annular structure. The annular structure has the advantage of being able to make the central space of the outside and inside a cooling space. The heat pipe has a structure as seen in the previous case, but its novelty stands out. Furthermore, this study realized one-dimensional modeling of the heat pipe by improving problems such as the modeling of a structure including wicks, which are disadvantages in heat pipe modeling that could not be seen in previous studies, and thus simplifies the implementation in CFD modeling. In Kapekov's case [26], there was a case in which heat pipes were partially simplified and modeled, but it was the first time that a complementary system was modeled in a CAHP. The design of the CAHP and the application of new one-dimensional modeling techniques in this study has not been seen in previous literature. Since these technologies have already been recognized for their value as patents [40], this novelty is sufficient.

The conventional heat pipe and CAHP are shown in Figure 1a,b. Comparing the conventional heat pipe with the CAHP, the conventional heat pipe transfers heat from the heat source to the heat sink, but the location of the adiabatic section of the CAHP is not clearly defined, which can greatly expand the condenser area. Figure 1 shows the heat-resistant network [20,21] of the conventional heat pipe and the CAHP. The CAHP's thermal resistance network shows a similar form between the evaporator and the condenser, but the flow characteristics of the working fluid inside are significantly different. In this study, the results of the one-dimensional analysis comparing experiments after the one-dimensional modeling of the CAHP using AMESIM were investigated. In addition, this study analyzes the heat transfer characteristics of the CAHP through experiments and 1-D modeling and attempts to predict the effects of various design factors (porosity, length, wick characteristics, and so on) of additional heat pipes through simulation.

2. Concentric Annular Heat Pipe

The CAHP used in the experiment and analysis is shown in Figure 1b. The CAHP with distilled water as a working fluid is 90 mm in length, 62 mm in inner diameter, and 70 mm in outer diameter.

As shown in Figure 2, to improve the convective heat transfer at the condenser region (inner surface), 48 fins were bonded by sintered silver pastes. The heater (20 mm × 20 mm) was installed in the middle of the outer surface, and the hollow region was cooled by an electric fan. The material of the container was stainless steel 304, and the material of the fins was electrolytic copper.

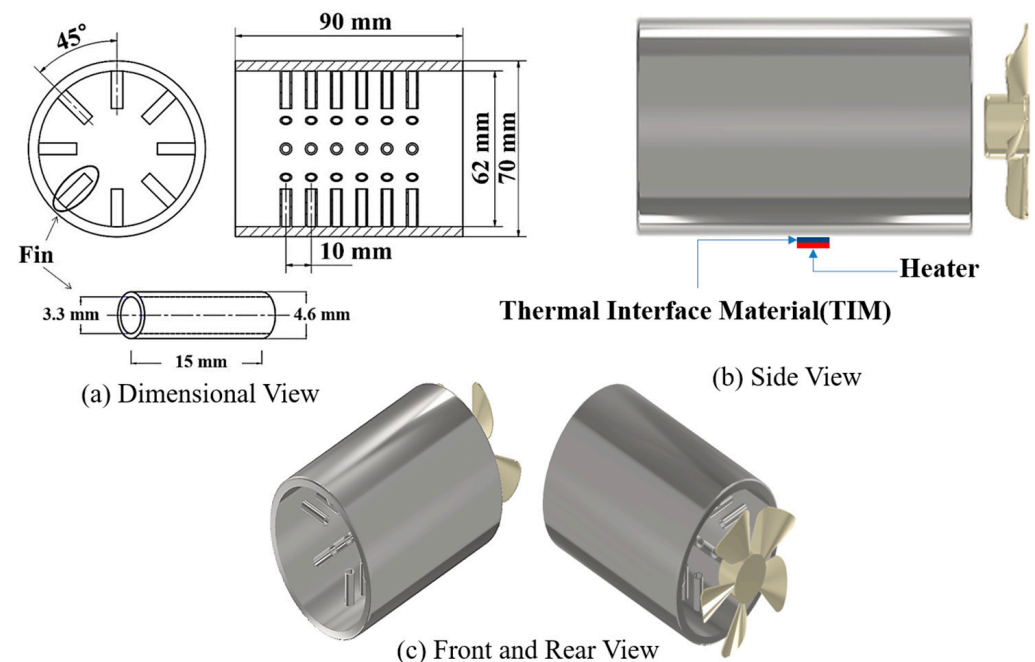


Figure 2. The design and shape of the CAHP.

A screen mesh wick (2-layered, 500 mesh, Stainless Steel 304) was installed in the internal outer surface, and the thickness of the wick was 0.34 mm. The material of the container was stainless steel 304, and the thickness of the tubes is 0.4 mm. The thermal properties of the CAHP are shown in Table 1.

Table 1. The thermal properties of the CAHP.

Material	Density [kg/m ³]	Thermal Conductivity [W/m ² K]	Specific Heat [J/kg-K]
Stainless steel 304	8000	16.3	530
Thermal Interface Material (TIM)	250	0.73	0.87
Heater (Si3N4)	3200	20	660

3. The Numerical Analysis Method

To analyze the CAHP by AMESIM, one-dimensional modeling was conducted with the following assumptions [41]:

- The wick structure is completely immersed;
- The flow in the wick is classified as Darcy's flow;
- If the flow in the wick is Darcy's flow and completely immersed, effective thermal conductivity can be applied to the wick structure;
- After condensation, the liquid film only occurs at the inner wall and wick;
- The contact resistance of the fin is neglected, and the adiabatic condition is applied to the end of the fin.

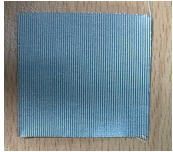
3.1. Effective Thermal Conductivity Model

If the wick is completely immersed and the flow in the wick is Darcy's flow, the wick structure can be used with effective thermal conductivity. The effective thermal conductivity is given by Equation (1) [4–6,41,42]:

$$k_{eff} = \frac{k_s(2 + k_l/k_s - 2\epsilon(1 - k_l/k_s))}{2 + k_l/k_s + \epsilon(1 - k_l/k_s)}, \quad (1)$$

where k_{eff} is the effective thermal conductivity, k_s is the thermal conductivity of the solid, k_l is the thermal conductivity of the liquid, and ϵ is porosity. Table 2 shows the effective thermal conductivity of the wick. Other effective thermal properties are specified in Table 2.

Table 2. Effective thermal conductivity of the wick [4–6,41,42].

Variables	Values
Wick (500 mesh, Stainless steel 304)	
k_s	16.3
k_l	0.659
ϵ	0.345
k_{eff}	13.74
ρ_s [kg/m ³]	8000
ρ_l [kg/m ³]	980.49
ρ_{wick} [kg/m ³]	5576
$C_{p,s}$ [J/kg-K]	530
$C_{p,l}$ [J/kg-K]	4138
$C_{p,wick}$ [J/kg-K]	1791

The effective density and heat capacity are computed by proportional weighting using Equations (2) and (3).

$$\rho_{eff} = (1 - \epsilon)\rho_s + \epsilon\rho_l \quad (2)$$

$$c_{p,eff} = (1 - \epsilon)c_{p,s} + \epsilon c_{p,l} \quad (3)$$

3.2. One-Dimensional Modeling of CAHP and Boundary Conditions

The working fluid of the heat pipe was set to be a mass fraction for a given mass of liquid and pressure. The heat pipe was initially at 25 °C and 0.25 bar (25,000 Pa). The specific enthalpy, entropy, and pressure were defined by a p - h diagram, and all parameters were automatically computed by AMESIM [41].

The filling ratio of the working fluid was 10% and 20%. The internal volume was 60 mL, and the total mass of the working fluid was 0.006 kg and 0.012 kg when the filling ratios were 10% and 20%. The total mass of the working fluid can be calculated by Equation (4). Based on the internal working fluid filling amount, the total filled mass was converted, and the liquid film thickness on the wall surface and t_{lf} were calculated inversely using Equation (4) [26,41] as shown in Table 3.

$$t_{lf} = \left[\frac{m_{fluid} - \rho_l \pi \epsilon (r_o^2 - (r_o - 2t_{wick})^2) L_{CAHP}}{\rho_l \pi L_{CAHP}} + r_i^2 \right]^{1/2} - r_i \quad (4)$$

Table 3. Thickness of liquid film in the CAHP according to volume fraction.

Volume Fraction [%]	Total Mass of Working Fluid [kg]	Thickness of Liquid Film [mm]
10	0.006	0.09
20	0.012	0.43
30	0.018	0.77
40	0.024	1.11
50	0.030	1.44
60	0.036	1.76
70	0.042	2.09
80	0.048	2.41

The heat was constantly supplied using the power supply, and the values were 10, 15, and 20 W, which were applied to the evaporator of the CAHP. The heat was transferred by conduction to the wick structure and by convection to the vapor, and the heat was then dissipated to the heat sink, which was the inner and outer wall of the CAHP. The thermal resistance network of the CAHP is shown in Figure 1b. Based on this network, the one-dimensional simulation model of the CAHP was performed by the Siemens Software (Munich, Germany), as shown in Figure 3. AMESIM can simulate multiple physical and multi-domain problems. AMESIM includes a variety of systems and functions: hydrographics, mechanics, electricity, two-phase flow, and signals. The model is solved using laws of physics or nonlinear time-dependent equations that depend on various correlations [41]. One-dimensional modeling has the advantage of being able to model a system in detail. Basically, it is based on the thermal resistance of the CAHP shown in Figure 1b but does not exactly enter the thermal resistance equation. Various components and physical factors constituting the CAHP can be implemented by sub-models of libraries embedded in AMESIM. As can be seen in Figure 3, the internal structure and flow characteristics of the CAHP are configured such that each library is connected one-dimensionally to constitute the system. The main libraries constituting the current CAHP model are presented in Table 4. Fluid circulation of the heat pipe may be simulated using different sub-models at each flow position where each library is arranged. One-dimensional modeling of the CAHP using AMESIM is designed to calculate the working fluid circulation using the built-in theoretical model of each library. Moreover, the AMESIM model has the advantage of being able to predict the dynamic characteristics of the system, and various predictions can be performed using internal functions that perform a wide range of calculations of various factors. The various equations to be used in each library of the CAHP model of Figure 3 are presented later. As illustrated in Figure 3, the blue element is from the two-phase flow library and represents vapor or liquid fluid flow. Chestnut brown represents the outer layer of the metal tube, which is a solid element constituting CAHP. It also represents a

self-defined, effective liquid–wick interface that is considered to have constant physical properties and heat exchange through conduction and convection. Red represents the signal elements required to provide physical interactions that are not automatically set in the AMESIM software. The sketch shown in Figure 3 includes a vapor line required for capillary pumping, an effective liquid–wick interface on the outer wall of the annular space, a condensed liquid line flowing along with the outer shell layer, and the wick and liquidity through the inner wall of the annular space. The ceramic heater (20 mm × 20 mm) and thermal interface material were drawn in the bottom center of the CAHP. Thermal properties were applied based on Table 2.

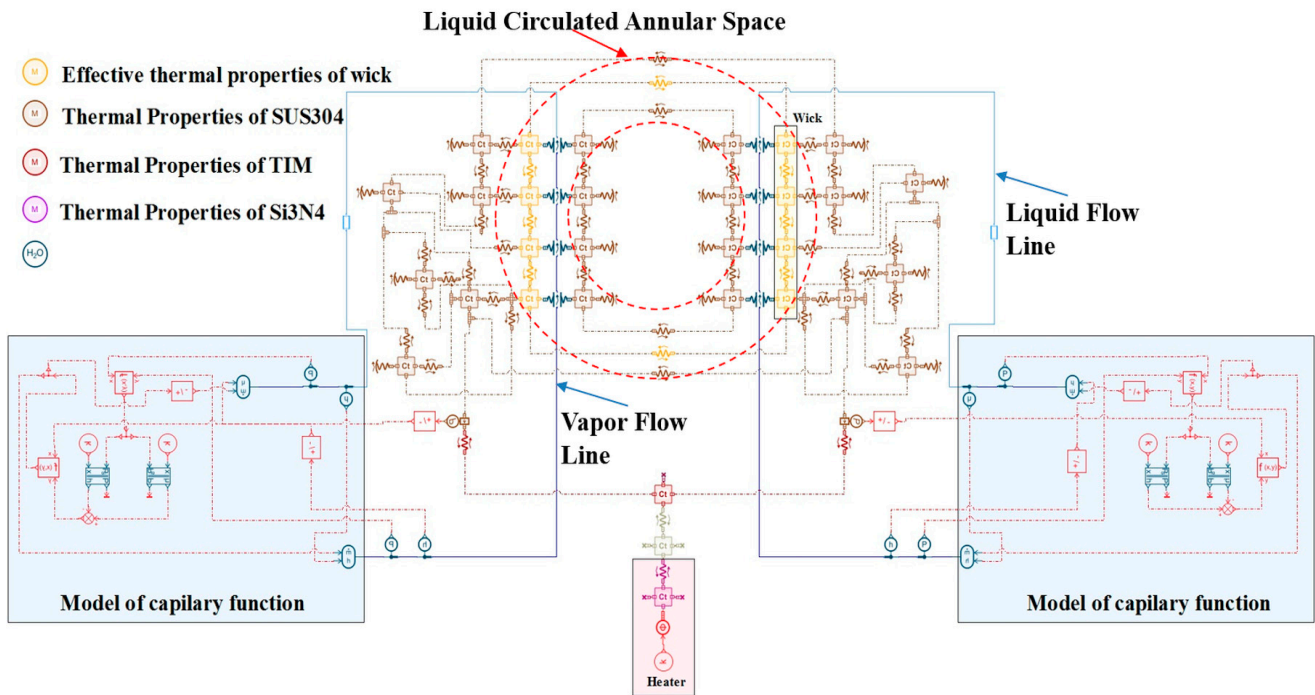


Figure 3. One-dimensional AMESIM modeling of the CAHP.

In the one-dimensional modeling, the mean pressure between the vapor line and the liquid line is computed by simulation, and this mean pressure artificially determines the flow of the CAHP, which is automatically computed and updated. From this process, the specific enthalpies, both h_l (fully liquid, $x = 0$) and h_v (fully vapor, $x = 1$), are computed, and the mass flow rate of CAHP can then be given as follows [26,41]:

$$l_v = h_v - h_l, \text{ and } \dot{m} = Q/l_v. \quad (5)$$

In the simulation, the conduction heat transfer between two materials is defined as follows [41–43]:

$$Q = \frac{1}{\frac{L_1}{k_1 A_1} + \frac{L_2}{k_2 A_2}} (T_2 - T_1), \quad (6)$$

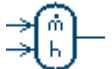
$$Q = \frac{1}{\frac{\ln\left(\frac{r_2}{r_1}\right)}{k_1 2\pi L_e} + \frac{\ln\left(\frac{r_3}{r_2}\right)}{k_2 2\pi L_e}} (T_2 - T_1). \quad (7)$$

The convective heat transfer is defined by Newton's cooling law [43]:

$$Q = hA(T_{surf} - T_\infty), \quad (8)$$

where h is the convective heat transfer coefficient, A is the area of the surface, T_{surf} is the surface temperature, and T_∞ is the atmosphere temperature.

Table 4. Main AMESIM library components used in the CAHP model.

Library Component	Component Name	Description	Library Component	Component Name	Description
	Transformer	thermodynamic state transformer		Thermal node	thermal temperature (fixed by port 4) and heat flow node
	Fluid properties	refrigerant thermodynamic properties with working fluids		Heat source	conversion of signal to a heat flow
	Modulated source	modulated mass and enthalpy flow rate source		External mixed convection	external mixed convective exchange with various convection models
	Fluid property sensor	generic sensor with additional thermodynamic state variable		Convective exchange	generic conduction
	Two-phase flow pipe volume	pipe with heat exchange with 2 thermal ports (C-R), related to various two-phase flow models		Thermal capacitance	thermal capacity
	Solid properties	thermal solid properties with various materials		Mathematical function	signal function of inputs x and y
	Power sensor	power/energy/activity sensor with offset and gain		Sign inverter	reverses the sign of the input
	Gain	outputs a signal with a constant specified value		Generic sensor	calculates additional thermodynamic state variables

The convective heat transfer coefficient is calculated by the Nusselt number, which is the function of the Prandtl number and the Grashof number given a free convection or the Prandtl number and the Reynolds number given a forced convection. The Nusselt number, Prandtl number, Grashof number, Rayleigh number, and Reynolds number are defined with Equations (9)–(14) [41,43]:

$$Nu = \frac{h \cdot L_c}{k}, \quad (9)$$

$$Pr = \frac{\mu \cdot C_p}{k}, \quad (10)$$

$$Gr = \frac{L_c^3 \cdot g \cdot \rho^2 \cdot \alpha \cdot |T_{wall} - T_{fluid}|}{\mu^2}, \quad (11)$$

$$Ra = Pr \cdot Gr, \quad (12)$$

$$Re = \frac{|V_{fluid}| \cdot L_c}{\mu / \rho}. \quad (13)$$

The function of the Nusselt number is defined by Equations (14)–(16) [41–43].

For free convection (Churchill and Chu),

$$Nu = \left[0.825 + \frac{0.387(Gr \cdot \sin\theta \cdot Pr)^{\frac{1}{6}}}{\left\{ 1 + (0.492/Pr)^{\frac{9}{16}} \right\}^{\frac{8}{27}}} \right]^2 \quad (14)$$

For forced convection with a laminar flow (Kreith and Black),

$$Nu = 0.664Re^{1/2}Pr^{1/3}. \quad (15)$$

For forced convection with a turbulent flow (Kreith and Black),

$$Nu = 0.037Re^{4/5}Pr^{1/3}. \quad (16)$$

The velocity of a two-phase flow is calculated by Equation (17):

$$V_{fluid} = \frac{\dot{m}}{A \cdot \rho_{vp}}, \quad (17)$$

where \dot{m} can be calculated using Equation (6)

The Nusselt number correlations (Gnielinski) of the single-phase flow are found by Equation (18) [41]:

$$Nu = \frac{\frac{f}{8}(Re - 1000)Pr}{1 + 12.7\sqrt{\frac{f}{8}} \cdot (Pr^{\frac{2}{3}} - 1)}. \quad (18)$$

The Nusselt number and heat transfer coefficient correlations of the two-phase flow are found with Equations (19)–(27) [41]:

For two-phase condensation (Shah correlation),

$$h_{TP} = h_{LO} \cdot \left[\left((1-x)^{0.8} + 3.8 \frac{x^{0.76} \cdot (1-x)^{0.04}}{(p/p_{cr})^{0.38}} \right) \right] \quad (19)$$

$$h_{LO} = 0.023Re^{0.8}Pr^{0.4} \frac{k_l}{D_h}. \quad (20)$$

For two-phase boiling (VDI Heat Atlas),

$$h = \sqrt[3]{h_{cv}^3 + h_{NcB}^3}. \quad (21)$$

h_{cv} and h_{NcB} can be calculated with Equations (22) and (26).

$$h_{cv} = h_{LO} \cdot F_{TP} \quad (22)$$

$$F_{TP} = \frac{1}{[A_1 + A_2]^{0.5}} \quad (23)$$

$$A_1 = (1-x)^{0.01} \cdot (1-x)^{1.5} + 1.9x^{0.6} \left(\left(\frac{\rho_l}{\rho_g} \right)^{0.35} \right)^{-2.2} \quad (24)$$

$$A_2 = x^{0.01} \cdot \left[\frac{h_{VO}}{h_{LO}} \left(1 + 8 \cdot (1-x)^{0.7} \cdot \left(\frac{\rho_l}{\rho_g} \right)^{0.67} \right) \right]^{-2} \quad (25)$$

$$h_{NcB} = h_{NcBO} \cdot F_{NcB}, \quad (26)$$

$$F_{NcB} = F_{PF} \left[\frac{\dot{q}}{\dot{q}_0} \right]^{nf} \left[\frac{D_h}{D_0} \right]^{-0.4} \left[\frac{R_p}{R_{p0}} \right]^{0.133} \left[\frac{\dot{m}}{\dot{m}_0} \right]^{0.25} \left[1 - p_{red}^{0.1} \left[\frac{\dot{q}}{q_{cr,PB}} \right]^{0.3} \right] \cdot x \cdot F(M), \quad (27)$$

where F_{PF} , \dot{q}_0 , h_{NcBO} , R_{p0} , m_0 , and $F(M)$ are constant parameters depending on the working fluid. $q_{cr,PB}$ is calculated by a given correlation embedded in AMESIM [41].

If the contact resistance of the fins is neglected and the adiabatic condition is applied to the end of the fin, Equations (28)–(30) can be used [43]:

$$\eta_f = \frac{\tanh(ML)}{ML}, \quad (28)$$

$$ML = \sqrt{\frac{hP}{kA_{fin,c}}} \cdot L, \quad (29)$$

$$\eta_{total} = 1 - \frac{A_{fin}}{A_{total}} (1 - \eta_{fin}), \quad (30)$$

where η_f is the efficiency of one fin, h is the convective heat transfer coefficient, P is defined as the perimeter of the fin, k is the thermal conductivity, $A_{fin,c}$ is the cross-sectional area of the fin, L is the length of the fin, η_{total} is the total efficiency of the fins, A_{fin} is the area of the fins, and A_{total} is calculated by $A_{fin} + A_{base}$.

The effective convective heat transfer area (A_{eff}) can be obtained with Equation (31), and A_{eff} can be applied to AMESIM by Equations (32) and (33) [41,43]:

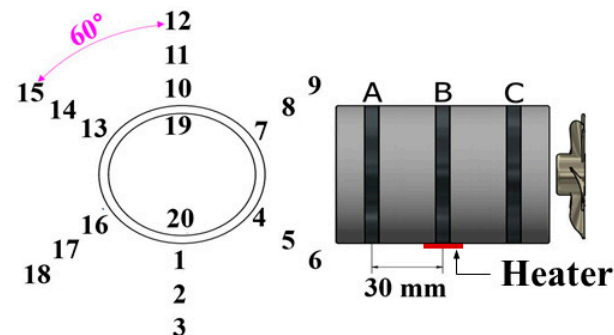
$$A_{eff} = A_{total} \cdot \eta_{total}, \quad (31)$$

$$K_{Heat} = \frac{A_{eff}}{A_{base}}, \quad (32)$$

$$Q = K_{Heat} \cdot A_{base} \cdot h \cdot (T_{wall} - T_{fluid}). \quad (33)$$

4. Experimental Equipment and Conditions

As shown in Figure 4, a ceramic heater (20 mm × 20 mm) was installed in the middle of the outer surface of the CAHP, and thermocouples (TC, K-type) were attached to 20 locations to measure the temperature. The working fluid used distilled water, and the temperature of the atmosphere was maintained at around 25 °C.



Thermocouple Position

A : 1, 4, 7, 10, 13, 16, 19, 20

B : 2, 5, 8, 11, 14, 17

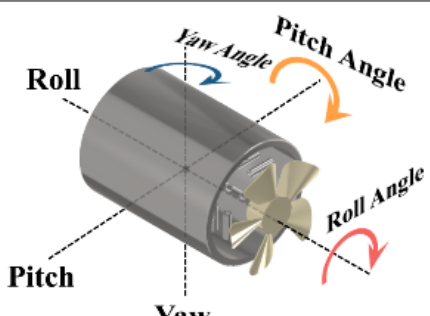
C : 3, 6, 9, 12, 15, 18

Heater : 2

Figure 4. Thermocouple positions of the CAHP.

As shown in Table 5, the experiment was conducted with various supplied power inputs, the airflow rate in the condenser region, the volume fraction of the working fluid, the pitch angle and roll angle of the CAHP as variables to evaluate the thermal characteristics and performance. The internal pressure of the CAHP was 25,000 Pa at absolute pressure.

Table 5. Variables of the experiment.

Variables	Values
Q : Heat In [W]	10, 15, 20
\varnothing : Volume Fraction [%]	10, 20
V_{air} : Air Flow Rate [m/s]	0, 1, 2, 3
	–30, –15, 0, 15, 30
	+ Angle(CCW) – Angle(CW)
Pitch Angle [°]	
	0, 15, 30
Roll Angle [°]	Roll Angle 
Definition of Concentric Annular Heat Pipe Orientation	

The volume fraction (filling ratio) of the working fluid is defined with Equation (34):

$$\varnothing = \frac{Vol_{water}}{Vol_{CAHP}} \times 100 [\%]. \quad (34)$$

The thermal resistance of the CHAP is calculated with Equation (35):

$$R_{th,HP} = \frac{T_h - T_{air}}{Q}. \quad (35)$$

As shown in Figures 4 and 5, the experimental system consisted of a CAHP, a heater, a cooling fan, a power supply, a charging syringe, and a data logger. The ceramic heater with a cross-sectional area of 20 mm × 20 mm and a thickness of 2 mm could operate at 50 V and 65 W or less. In addition, the heater was attached to the bottom surface of the evaporator through a thermal pad. The power supply connected to the heater was TOYOTECH's TDP-1005B model (TOYOTECH, Incheon, Korea), and the display accuracy was ±0.1% rdg. A cooling fan with an external diameter of 70 mm and an internal diameter of 65 mm was used and operated within the ranges of DC 12 V and 0.7 A. The speed was adjusted to the power supply (Wanjun KSM400-1) connected to the cooling fan. The speed of the cooling fan was measured using an anemometer (Testo 405i, Testo, Titisee-Neustadt, Germany), and the accuracy of the speed measurement was ±5% rdg + 0.1 m/s. The vacuum pump used was a Value FY-4C-N model (VALUE, Zhejiang, China), which can be vacuumed at a

flow rate of $14.4 \text{ m}^3/\text{h}$ and a maximum partial pressure of 2 Pa. In addition, the minimum scale of the charging syringe was 1 mL. The filling ratio uncertainty was $\pm 0.25\%$ of the visibility error of the charging syringe. The data logger was the Yokogawa MX100 model (Yokogawa, Tokyo, Japan), and the measurement error rate of the K-type thermocouple was $\pm 0.05\%$ rdg. The thermocouple used was a K-type and could be measured at -200 and $1250 \text{ }^\circ\text{C}$ due to the Seebeck effect. The measurement error rate of the thermocouple was $\pm 0.75\%$. The total uncertainty retrieved from the thermal resistance was calculated as $\pm 0.027\%$ by the methods of [44,45] with Equations (36) and (37). The uncertainty of the heat supplied to the CAHP was $\pm 0.27\%$. Equation (36) defines the uncertainty of the heating power, and Equation (37) defines the thermal resistance.

$$w_Q = \left[\left(\frac{\partial P}{\partial V} w_V \right)^2 + \left(\frac{\partial P}{\partial I} w_I \right)^2 \right]^{1/2} \quad (36)$$

$$w_R = \left[\left(\frac{\partial R}{\partial Q} w_Q \right)^2 + \left(\frac{\partial Q}{\partial(\Delta T)} w_{(\Delta T)} \right)^2 \right]^{1/2} \quad (37)$$

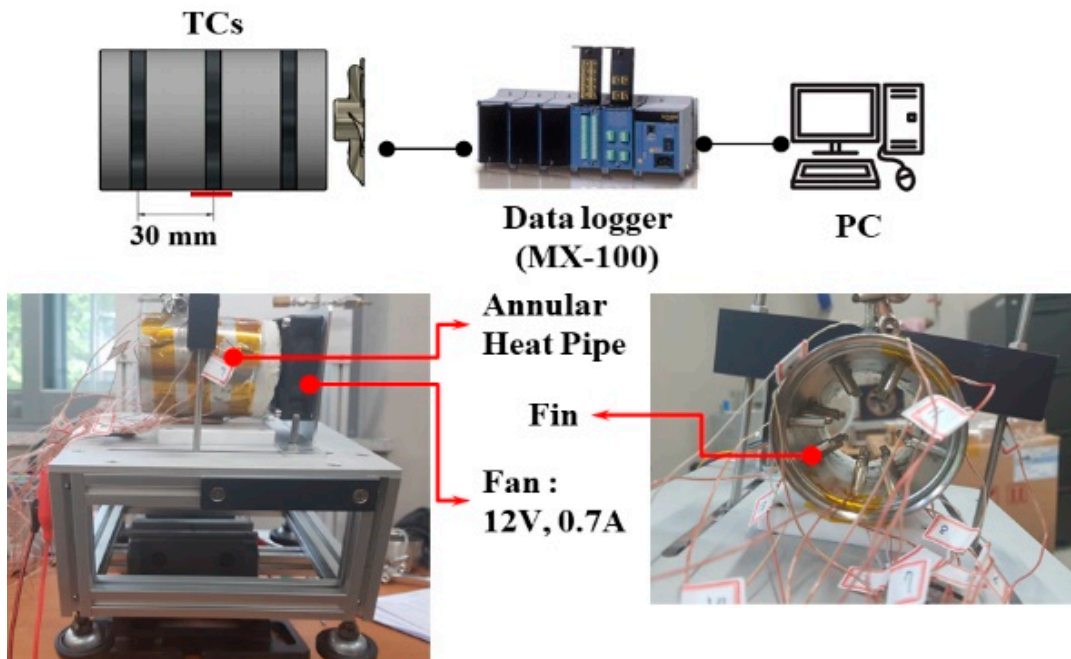


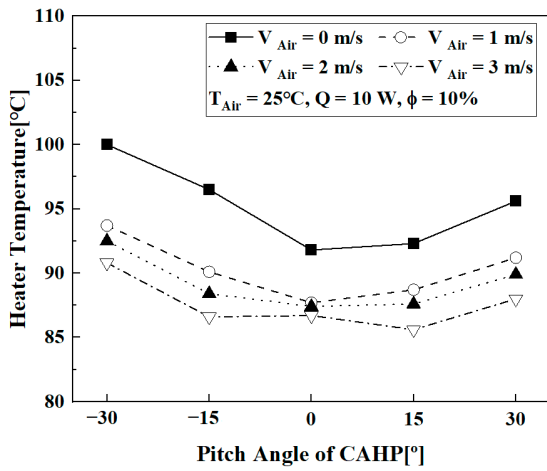
Figure 5. Experimental equipment of the CAHP.

5. Results and Discussions

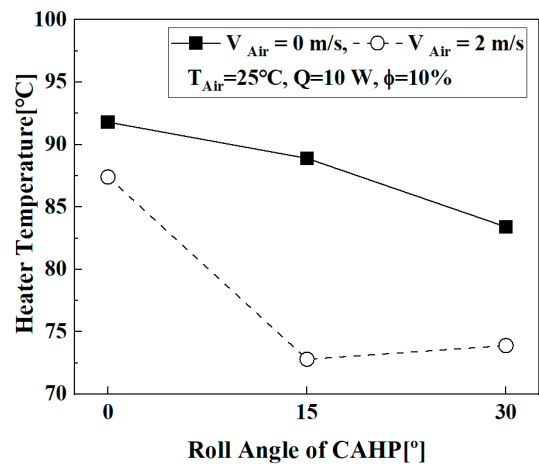
5.1. Experimental Results

The experiments on the performance and characteristics of the CAHP were conducted by changing the variables. The experimental variables include the heating value (Q), the volume fraction of the working fluid (\varnothing), the airflow velocity (V_{air}) in the capacitor part, the pitch angle, and the roll angle, and the results are as follows. The heater temperature, pitch angle, and roll angle according to Q when $\varnothing = 10\%$ are shown in Figure 5. Figure 6a–f shows the effect of orientation with pitch and roll angle on heater temperature of $\varnothing = 10\%$. When Q was 10 W, the pitch angle was 15° , V_{air} was 3 m/s, and the heater temperature was $85.6 \text{ }^\circ\text{C}$, the lowest in Figure 6a. As shown in Figure 6c,e, the heater temperature tended to be similar. However, as shown in Figure 6e, if the pitch angle was 0° , the heater temperature rose even if the convective heat transfer was improved through the cooling fan. It can be seen that the temperature was somewhat lower in the case of natural convection than in

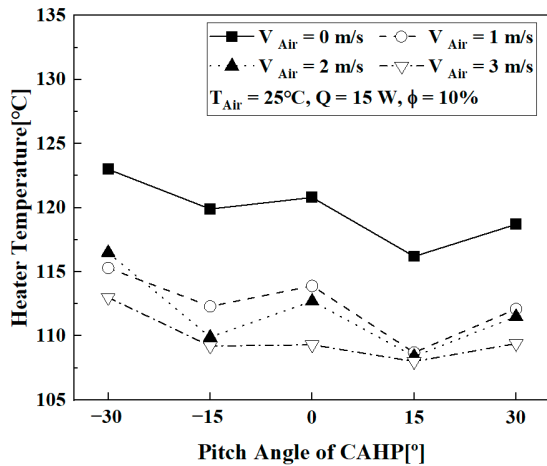
the case where the flow velocity was 1 m/s. It was expected that the internal abnormal flow characteristics were partially affected by the flow velocity.



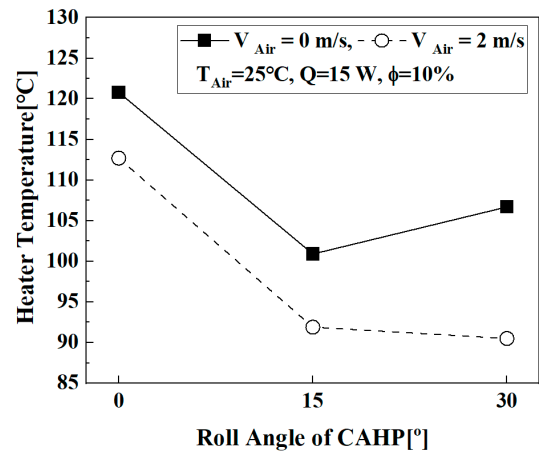
(a) Effect of Pitch Angle, $Q = 10$ W



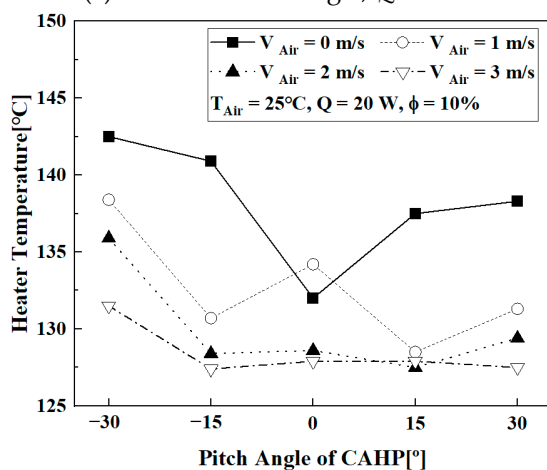
(b) Effect of Roll Angle, $Q = 10$ W



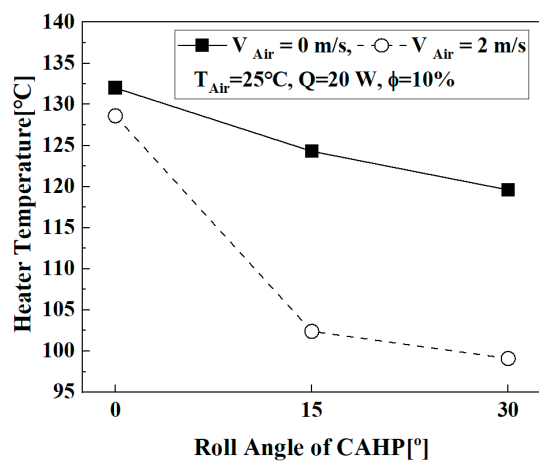
(c) Effect of Pitch Angle, $Q = 15$ W



(d) Effect of Roll Angle, $Q = 15$ W



(e) Effect of Pitch Angle, $Q = 20$ W



(f) Effect of Roll Angle, $Q = 20$ W

Figure 6. Heater temperature according to Q , V_{air} , pitch angle, and roll angle ($\varnothing = 10\%$).

When the pitch angle was from -15° to 15° , the performance of the CAHP was not significantly different, but the heater temperature increased significantly at -30° and 30° pitch angles. Considering the significant increase in heater temperature, the CAHP did not

appear to work when the pitch angle was -30° and 30° . Figure 6b,d,f show that the heater temperature tended to decrease as the roll angle rose, except, as shown in Figure 6d, with a 15° roll angle and free convection. When 15 W was supplied to the CAHP at a roll angle of 15° , unlike the supply heat of 10 and 20 W, the heater temperature was lower than it was at a 30° roll angle, which seems to be a measurement error.

Considering the results according to the roll angle, the best operating condition of the CAHP was a roll angle of 30° and a V_{air} of 2 m/s.

As shown in Figure 6, the heater temperature according to pitch angle when $\phi = 10\%$ had a lower temperature with a 15° pitch angle than when the pitch angle was 0° . This result means that the working fluid was circulated actively as the CAHP was tilted at a 15° pitch angle. However, when the pitch angle was -30° and 30° , the heater temperature was remarkably increased. This is because the working fluid did not reach the evaporator when the CAHP was tilted at a 30° pitch angle as in the case of $\phi = 10\%$, shown in Figure 7a. In accordance with the roll-pitch inclination angle of the CAHP, the surface of the internal evaporation area became dry without the working fluid, making it difficult to operate the CAHP. It can be seen that, even if a wick is installed inside, the capillary force cannot sufficiently transfer the liquid to the evaporation area. Therefore, the capacity and direction in which the evaporation region is always wet with fluid should be maintained as shown in Figure 7b.

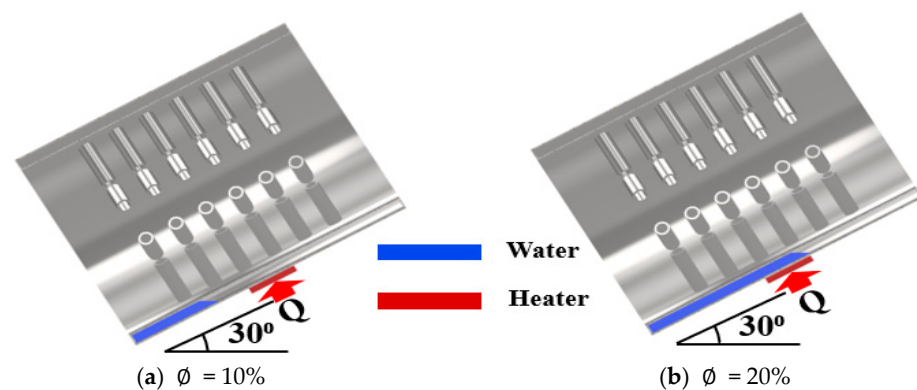
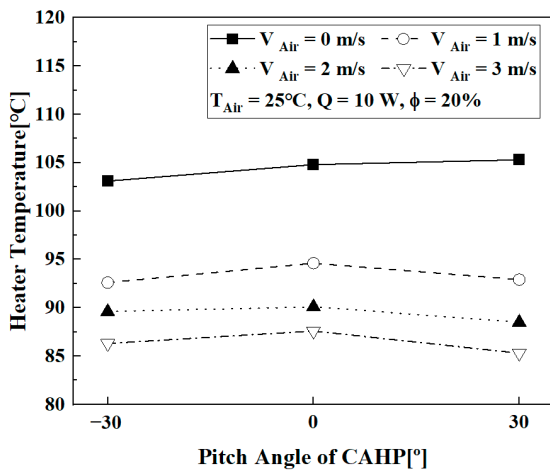


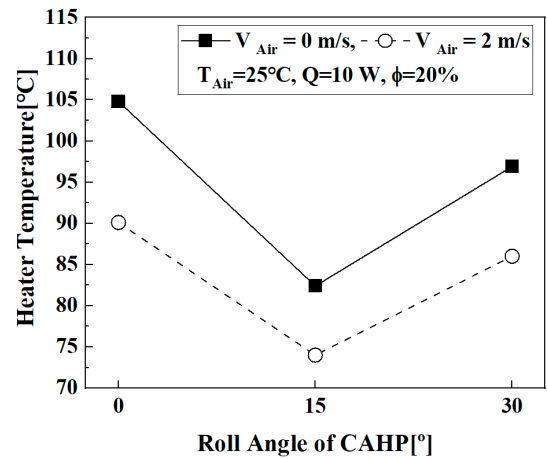
Figure 7. Location of working fluid at different charged ratios with a pitch angle of 30° .

Figure 8 shows the heater temperature of the CAHP according to the influence of various environmental variables. This shows the results of the experiment when $\phi = 20\%$. Referring to Figure 8a,b, the heater temperature was 85.3°C at $Q = 10\text{ W}$, pitch angle = 30° , and the heater temperature was 82.4°C at $V_{air} = 3\text{ m/s}$. This shows that, as shown in Figure 8a,c,e, proper operation at a 30° pitch angle requires more than 20%, which is the capacity for the evaporation to be sufficiently wet, as shown in Figure 8. Unlike the previous results in Figure 6, the heater temperature decreased as convective heat transfer improved, which can be seen in all the results in Figure 8a,c,e. The heater temperature according to the roll angle when $\phi = 20\%$ is shown in Figure 8b,d,f. In this case, the minimum heater temperature was observed to be inclined with a 15° roll angle. Regardless of Q or V_{air} , the optimal operating condition of the CAHP can be concluded to be 15° .

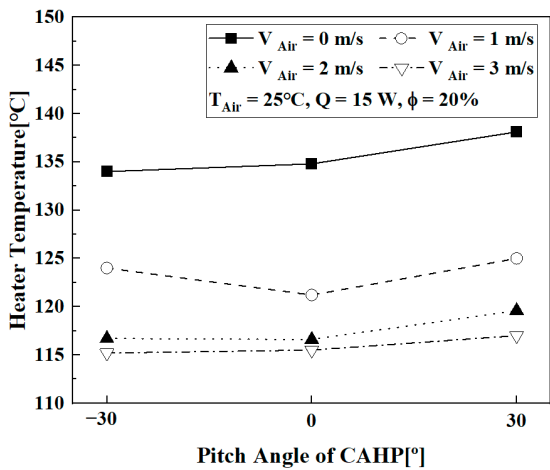
Figures 6 and 8 show the effect of the roll angle on the CAHP. Figure 8 clearly shows that the optimal operating condition is when the CAHP is tilted at a 15° roll angle. This is not definitely conclusive, but when the roll angle is 15° , it can be assumed that the vapor has an optimal 3-D flow in the CAHP.



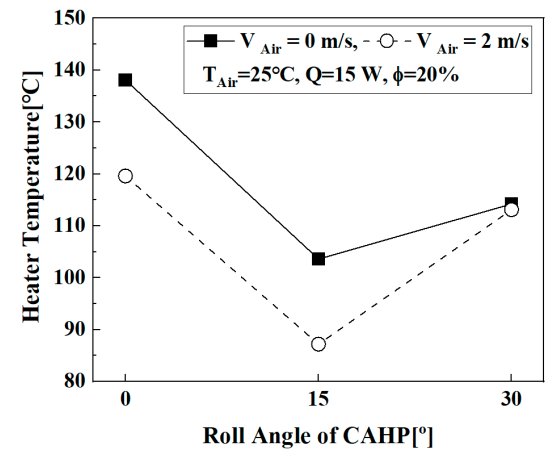
(a) Effect of Pitch Angle, $Q = 10$ W



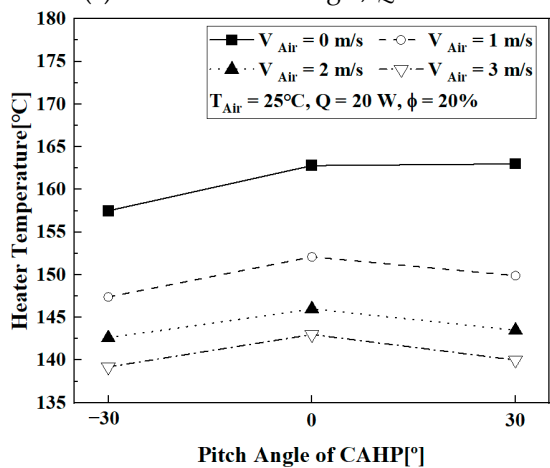
(b) Effect of Roll Angle, $Q = 10$ W



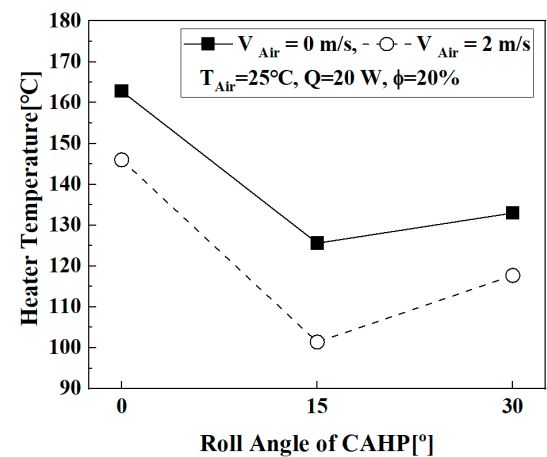
(c) Effect of Pitch Angle, $Q = 15$ W



(d) Effect of Roll Angle, $Q = 15$ W



(e) Effect of Pitch Angle, $Q = 20$ W



(f) Effect of Roll Angle, $Q = 20$ W

Figure 8. Heater temperature according to Q , V_{air} , pitch angle, and roll angle ($\phi = 20\%$).

Figure 9a shows the heater temperature (T_H), condenser temperature (T_C), and thermal resistance (R_{th}) of the CAHP, which can be calculated by Equation (35), according to the heating load in the best working condition. In this case, when Q increased, the temperature of the heater and condenser increased, the thermal resistance of the CAHP decreased, and the minimum value of the thermal resistance was 3.74 °C/W when Q was 20 W, V_{air} was 3 m/s, the pitch angle was -15° , and ϕ was 10% . As shown in Figure 9a, as the pitch

angle changed, it was easier for the internal vapor rise to be transmitted upward in the axial direction. Since the pitch angle is symmetrical based on the center to which the heater is attached, it is expected to help the vapor rise from -15° to 15° . It can be seen that the flow direction of the working fluid inside the CAHP varied greatly depending on the tilt direction and angle. Figure 9b compares the thermal resistance of the CAHP performed in this study with the thermal resistance of a heat pipe in previous literature. This research compares the CAHP with the previous basic heat pipe case, and between the heater and cooling air, they are similar in terms of thermal resistance. This research compares the thermal resistance of only a single tubular heat pipe, so the thermal resistance to the system obtained in this study was somewhat large. Based on the research results obtained from the current study, this can be improved by designing an optimal operating structure considering internal flow characteristics.

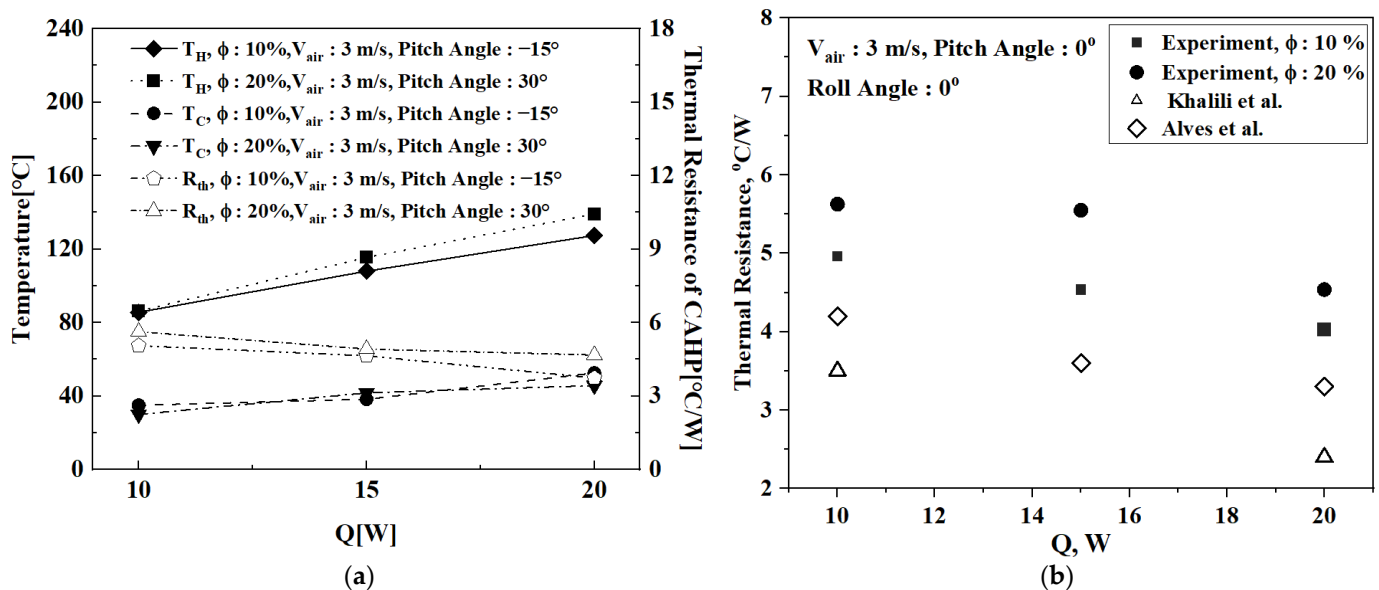


Figure 9. Temperature of the heater and the condenser and the thermal resistance of the CAHP according to Q . (a) Experimental characteristics. (b) Thermal resistance comparison with results from the literature.

5.2. Comparison between the Experiment and Simulation on Transient Temperature Variation

The experimental and simulation results for the temperature distribution of the CAHP according to time are shown as Figure 10a,b ($\phi = 10\%$, $V_{air} = 3$ m/s, $Q = 20$ W, pitch angle = 0° , and roll angle = 0°) and Figure 10c,d ($\phi = 20\%$, $V_{air} = 3$ m/s, $Q = 20$ W, pitch angle = 0° , and roll angle = 0°).

Comparing Figure 10a,b in the case of $\phi = 10\%$, the experimental results show that the heater temperature (T_2) was converged at 127.9 °C and that the condenser temperature (T_{19}) was converged at 41.4 °C, and the 1-D simulation results show that T_2 was converged at 123.6 °C and that T_{19} was converged at 32.9 °C. Using Equation (35), the thermal resistance of the CAHP can be calculated, and the results are 4.33 °C/W in the experiment and 4.53 °C/W in analysis, which are highly similar.

From Figure 10c,d in the case of $\phi = 20\%$, the results of the experiment and simulation can be compared as above. T_2 was converged at 143 °C in the experiment and at 143.8 °C in the analysis, and T_{19} was converged at 40 °C in the experiment and at 33 °C in the analysis. Based on these results, thermal resistance was calculated, and the results were 5.15 °C/W in the experiment and 5.54 °C/W in the simulation.

Comparing the experiment and simulation of the transient temperature distribution, the tendency to be converged was sharper in the analytical results than in the experimental results, but the overall trends of the temperature distribution and thermal characteristics of the CAHP can be verified as similar in the experiment and the analysis.

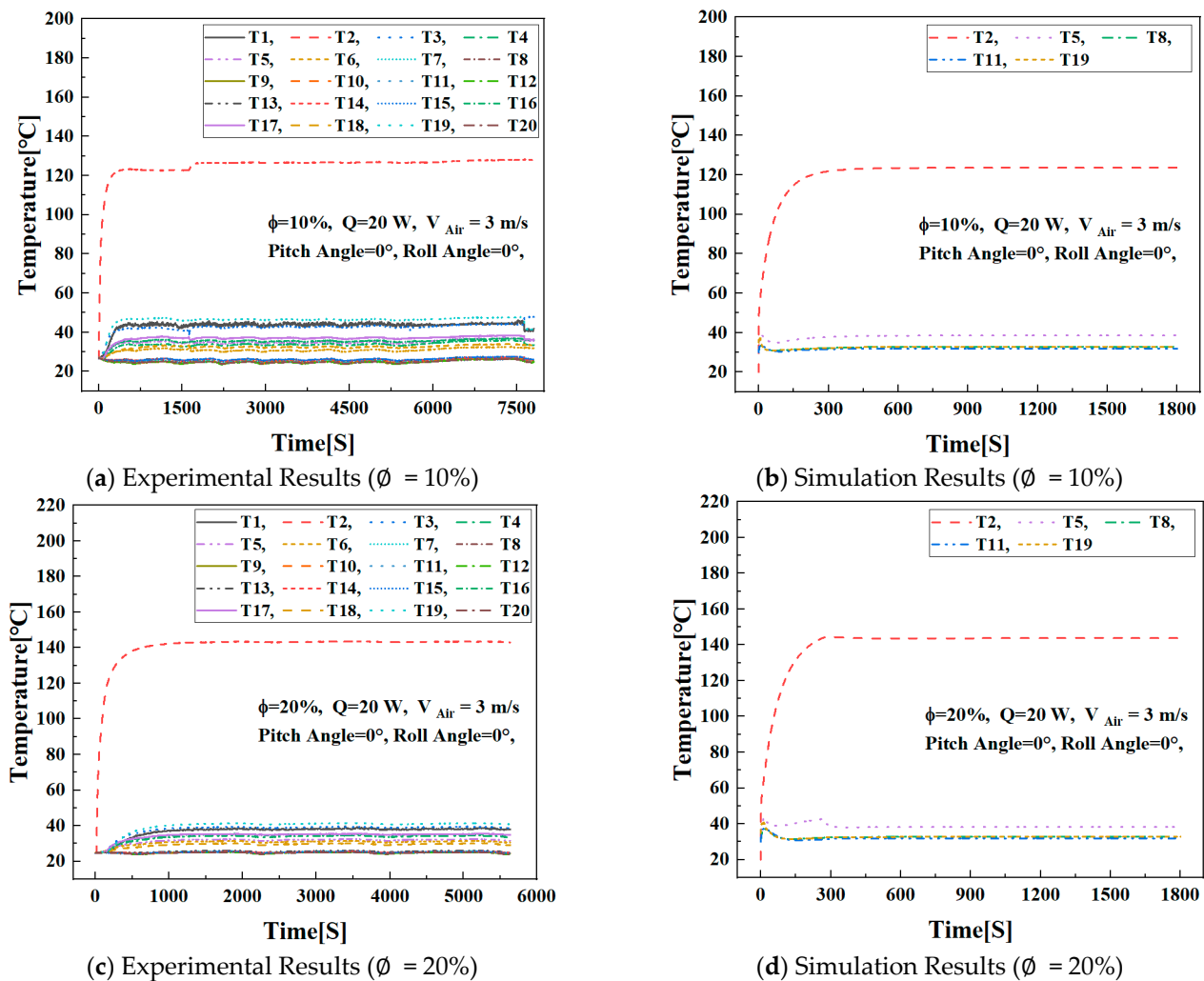


Figure 10. Transient temperature distribution of the CAHP ($V_{\text{air}} = 3 \text{ m/s}$, $Q = 20 \text{ W}$, pitch angle = 0° , and roll angle = 0°).

5.3. Comparison between the Experiment and Simulation on Thermal Performance

Figure 11 shows the comparison between the one-dimensional simulation results and the experimental results when the pitch angle and the roll angle are 0° . The heater temperature difference between the simulation and the experiment under the conditions of $Q = 20 \text{ W}$, $\phi = 10\%$, and $V_{\text{air}} = 0 \text{ m/s}$ was up to $8.64 \text{ }^\circ\text{C}$, and the error rate was 6.5%. As shown in Figure 11a–c, when comparing the experimental results with the calculated values of the one-dimensional model through AMESIM modeling, it can be seen that there is a slight difference given a capacity of 10%. As shown in the figure, the calculated values for $Q = 10$ and 20 W show lower temperatures than the experimental values. In the case of $Q = 15 \text{ W}$, on the contrary, the calculated value shows a higher value. This does not seem to satisfactorily match the heat transfer characteristics of the conditions of all results of the experimental conditions. As shown in Figure 11a, it can be seen that the experimental results and the simulation values are generally close, except when $Q = 0 \text{ W}$.

In Figure 11d–f, the experimental and simulation results show the results when $\phi = 20\%$. It can be confirmed that one-dimensional simulation using AMESIM is designed to suit the experiment well. Except under natural convection conditions as shown in Figure 11c, AMESIM results are close to the experimental results and can be predicted by the thermal characteristics of the CAHP. Figure 11 shows that it is possible to model the internal flow of a one-dimensional annular heat pipe through AMESIM by connecting resistors.

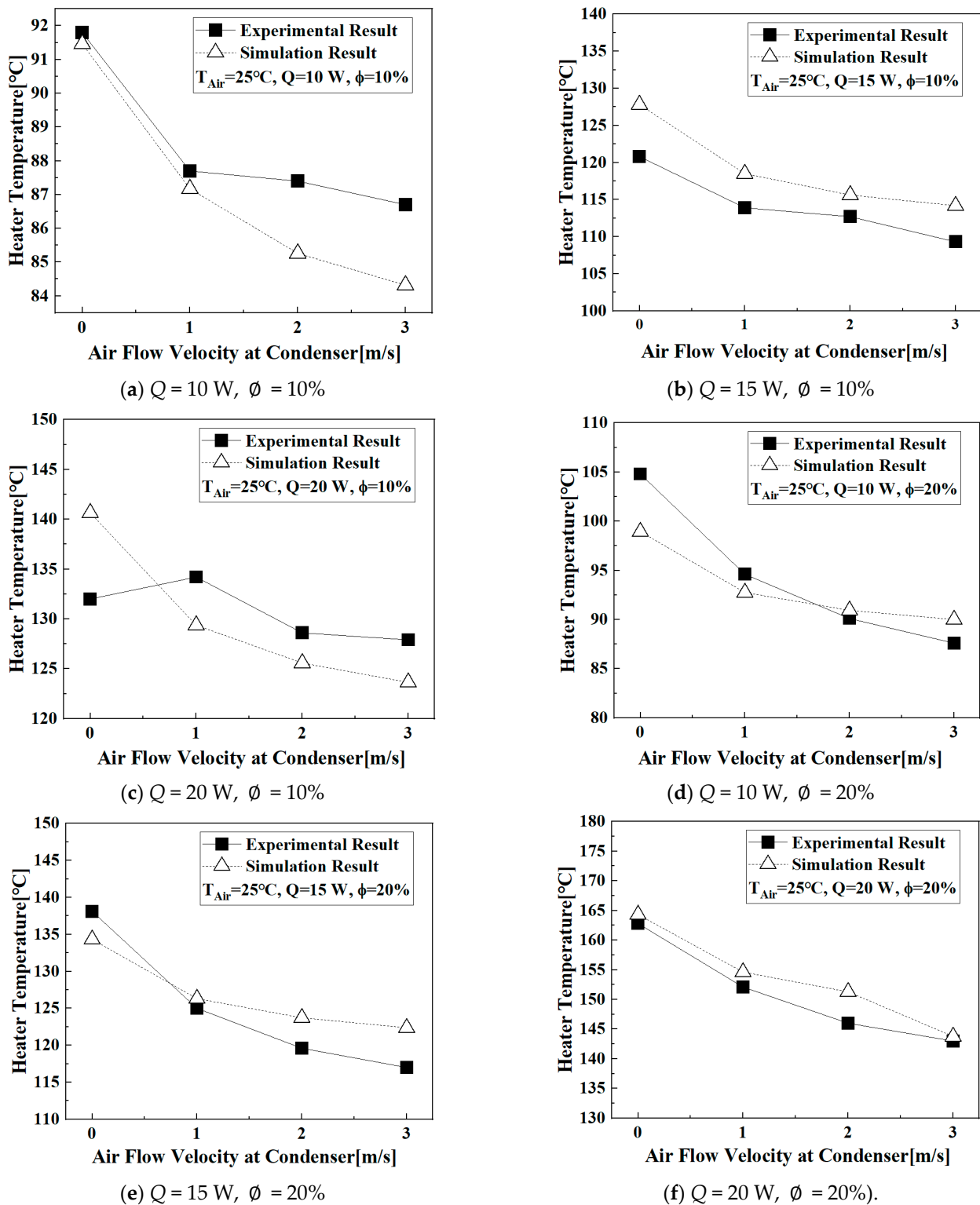


Figure 11. Comparison of experimental and simulation results regarding the effect of the airflow rate on the heater temperature according to ϕ , Q , and V_{air} (pitch angle = 0° , and roll angle = 0°).

5.4. Investigation for Thermal Characteristics of CAHP Using One-Dimensional Analysis

Case studies were conducted under various environmental conditions to find the thermal characteristics of the CAHP using the AMESIM simulation model. The effect of changes in the filling amount on the CAHP is shown in Figure 12. The results show that the thermal characteristics of the CAHP were greatly influenced by the volume fraction,

and the heater temperature varied according to the change in the volume fraction. The CAHP had a maximum heating temperature of 143.77 °C when $\phi = 30\%$ and a minimum heating temperature of 123.64 °C when $\phi = 10\%$. Based on these results, it was possible to determine the optimal volume ratio of the CAHP to be 10%. Generally, an optimal filling amount of a CAHP shall ensure a space in which internal vapor rises to the condenser and is condensed to return to the evaporator space, and, due to the nature of the internal wick, a condensate of an appropriate capacity shall flow through the capillary force of the wick.

This can be a continuous circulation structure inside the heat pipe. Therefore, the optimal capacity must be filled, which varies depending on the structure of the CAHP, so the optimal amount of working fluid filling must always be determined through experimental or theoretical analysis. In this study, based on the previous study case of Song et al. [21], the experiment was conducted by selecting 20% of the filling amount as the optimal capacity, but theoretical analysis confirmed that there was another temperature drop from 40%, so it was appropriate to select 20%.

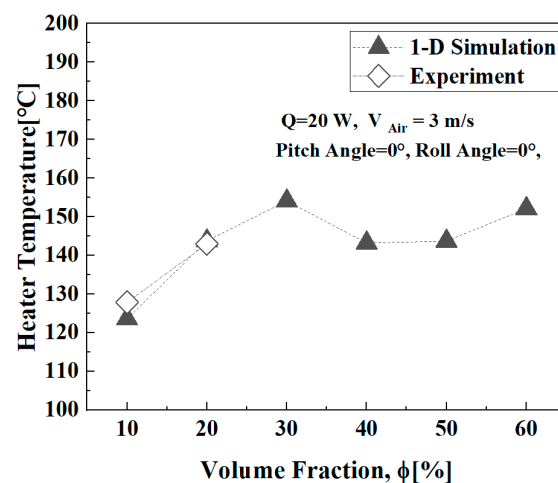


Figure 12. Simulated heater temperature according to the volume fraction of the CAHP ($V_{air} = 3$ m/s, $Q = 20$ W, pitch angle = 0°, and roll angle = 0°).

The effect of length on CAHP was studied through simulation, and the results are shown in Figure 13. Since it is impossible to change the length of the current experimental device, the effect of additional length was predicted through simulation. As shown in Figure 13, the length change (70–130 mm) showed that the heater temperature dropped slightly at a flow rate of 3 m/s. This was judged to have the lowest thermal resistance of CAHP when the flow rate is 3 m/s, so the additional resistance reduction effect is insignificant.

A simulation to find the effects of the wick structure was also conducted with the wick porosity and the number of layers. Figure 14 shows the thermal characteristics of the CAHP according to wick porosity. The thermal resistance of the CAHP changed little when the wick porosity was 0.3–0.7, but when the wick porosity was 0.1, 0.2, and 0.8, increasing trends of thermal resistance were found. The optimal wick porosity was 0.345, and the thermal resistance of the CAHP was 4.54 °C/W. In general, the higher the porosity of the wick of a CAHP, the larger the space in which the condensed liquid can penetrate, so it can improve the performance of the CAHP. However, since the capillary force through the wick inside the CAHP played a role in making the condensate precious to the evaporator section, the optimal wick porosity that can maintain space while maximizing the capillary force was verified through experiments. However, in this study, since a 500 mesh two-layer screen wick was used, it was difficult to confirm the characteristics of the wick because additional CAHP production is difficult. As specified by the experimental wicks installed in the current CAHP in Table 2, the porosity was 0.345, and the calculated value of 34% of this 1-D calculation was considered to be an appropriate value.

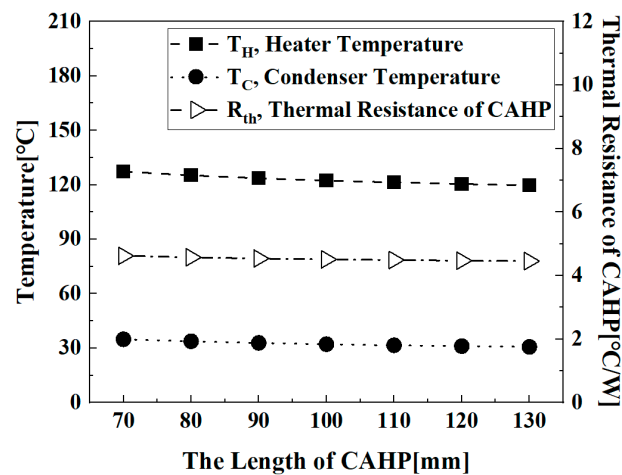


Figure 13. Simulated Thermal Characteristics of the CAHP according to length ($V_{air} = 3$ m/s, $Q = 20$ W, pitch angle = 0° , and roll angle = 0°).

Figure 15 shows the thermal resistance of the CAHP according to the layers of the wick (thickness of one layer = 0.34 mm). The thermal resistance of the CAHP was slightly down as the number of layers changed from two to four, but this does not significantly affect thermal performance. When the number of layers was one and five, the thermal resistance of the CAHP rose to comparable conditions. The optimal number of wick layers was four, and at that time, the thermal resistance was 4.47 $^\circ\text{C}/\text{W}$. However, the number of layers of the wick inside the heat pipe can be approached from the same point of view as the effect of the porosity of the wick in Figure 14. As the number of layers of the wick increased, the area in which the condensate can circulate increased according to the capillary force made in the wick. However, on the contrary, as the number of layers of the screen wick increased, the thickness of the wick increased, which soon reduced the flow space of the vapor, affecting the performance of the CAHP. The current CAHP installed a wick with two layers, and as illustrated in Figure 15, the effect of an increase in three–four layers was insignificant, so it seemed appropriate to choose a case with two layers.

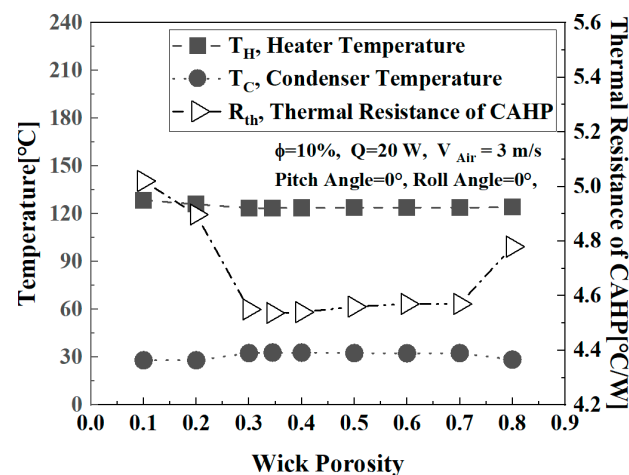


Figure 14. Simulated thermal characteristics of the CAHP according to wick porosity ($V_{air} = 3$ m/s, $Q = 20$ W, pitch angle = 0° , and roll angle = 0°).

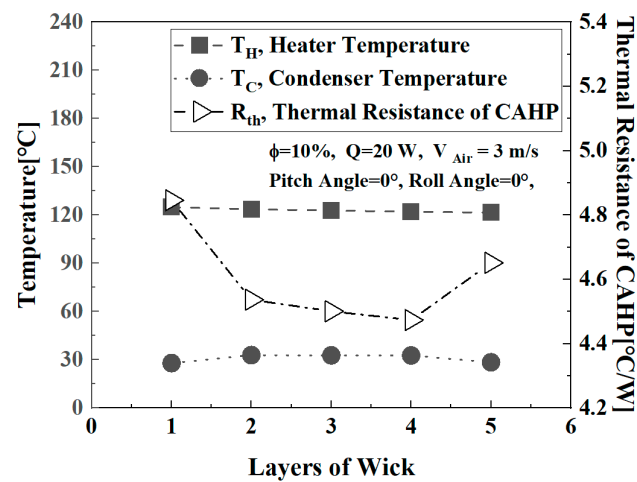


Figure 15. Simulated thermal characteristics of the CAHP according to the layers of the wick ($V_{air} = 3\text{ m/s}$, $Q = 20\text{ W}$, pitch angle = 0° , and roll angle = 0°).

6. Conclusions

In the current study, concentric annular heat pipes (CAHPs) were experimentally studied under various conditions, and the results were compared and verified by one-dimensional modeling. The operating characteristics were analyzed by applying a heat pipe with an annular structure that had not been applied before as a heat sink. The capacity of the working fluid inside the CAHP, the amount of heat supplied, the flow rate of the cooling air, and the operating characteristics according to the inclination in various directions could be confirmed.

If the filling amount was 10%, it was observed that the orientation had a large impact. This is believed to be due to the partial drying of the surface inside the evaporator.

If the amount of heat supplied increased, the thermal resistance of the CAHP decreased. When Q was 20 W, the lowest value was $3.74\text{ }^\circ\text{C/W}$.

The experimental results showed that the performance of the CAHP was best when the roll angle was 15° and the internal vapor flow was improved. However, in the one-dimensional modeling, it was difficult to implement a structure in which the entire system changed its position at various angles, and its performance was compared only with modeling in a vertical state.

As a result of verifying the simulation model by comparing the transient temperature variation between the experiment and the one-dimensional simulation, the similarity between the experiment and the analysis was verified. The modeling reliability was validated through comparison and verification between the 1-D AMESIM modeling and the experimental results, and it was possible to predict the thermal characteristics of the CAHP depending on factors such as porosity, length, and wick characteristics.

Author Contributions: H.-I.C. and H.-C.L. carried out the experiment. J.-S.L. and J.-H.A. performed numerical investigation and analysis. S.-H.R. carried out validation, project supervision, writing, and funding. All authors have read and agreed to the published version of the manuscript.

Funding: This research received no external funding.

Institutional Review Board Statement: Not applicable.

Informed Consent Statement: Not applicable.

Data Availability Statement: Not applicable.

Conflicts of Interest: The authors declare no conflict of interest.

Nomenclature

A	Area, m ²
C_p	Specific heat capacity, J/kg·°C
F	Correction factor
f	Fiction coefficient
Gr	Grashof number (dimensionless)
h_v	Specific enthalpy of vapor, J/kg
h_l	Specific enthalpy of liquid, J/kg
h	Convective heat transfer coefficient, W/m ² ·°C
k	Thermal conductivity, W/m·°C
L	Length, m
L_{CAHP}	Length of CAHP, m
l_v	Latent heat of fluid, J/kg
M	Convection variables in fin efficiency equation in Equations (28) and (29)
m_{fluid}	Total mass of the working fluid, kg
\dot{m}	Mass flow rate, kg/s
Nu	Nusselt number (dimensionless)
P	Perimeter of fin, m
p	Static pressure, N/m ²
Pr	Prandtl number (dimensionless)
Q	Heat transfer rate, W
\dot{q}	Heat flux, W/m ²
R_{th}	Thermal resistance, °C/W
Ra	Rayleigh number (dimensionless)
Re	Reynolds number (dimensionless)
R_p	Absolute Roughness, m
r_o	Radius of internal outer surface of CAHP, m
r_i	Radius of internal inner surface of CAHP, m
T	Static temperature, °C
t	thickness, m
V	Volume, m ³
V_{air}	Cooling air velocity, m/s
V_{fluid}	Velocity of two phase flow, m/s
w	Uncertainty of variables.
x	Quality
Greek	
ϵ	Porosity, V_{liquid} / V_{total}
η	Fin efficiency
μ	Dynamic viscosity, kg/m·s
ρ	Density, kg/m ³
ρ_{vp}	Density of working fluid in two phase velocity, kg/m ³
\emptyset	Volume fraction of charged working fluid, $(V_{Working Fluid} / V_{Total Volume}) \times 100$
Subscripts	
∞	Surrounding air
0	Reference
a	Adiabatic
Air	Cooling air
$base$	Fin base
c	Condenser
cr	Critical
cv	Convective boiling
eff	Effective
f	Fin, or fluid
f,c	Fin cross sectional
g	Vapor, or denoted as v
l	Liquid
lf	Liquid film

<i>LO</i>	Liquid only
<i>h</i>	Hydraulic
<i>HP</i>	Heat pipe
<i>NcB</i>	Nucleate boiling
<i>Q</i>	Heat load
<i>R</i>	Resistance
<i>s</i>	Solid
<i>surf</i>	Surface
<i>red</i>	Reduced
<i>TP</i>	Two-Phase
<i>VO</i>	Vapor only
<i>wick</i>	Wick

References

1. He, Z.; Yan, Y.; Zhang, Z. Thermal management and temperature uniformity enhancement of electronic devices by micro heat sinks: A review. *Energy* **2021**, *216*, 119223. [[CrossRef](#)]
2. IEA. *World Energy Outlook*; OECD; IEA: Paris, France, 2020.
3. Zhang, X.; Kong, X.; Li, G.; Li, J. Thermodynamic assessment of active cooling/heating methods for lithium-ion batteries of electric vehicles in extreme conditions. *Energy* **2014**, *64*, 1092–1101. [[CrossRef](#)]
4. Faghri, A. *Heat Pipe Science and Technology*; Taylor and Francis: Washington, DC, USA, 1995.
5. Reay, D.A.; Kew, P.A.; McGlen, R.J. *Heat Pipes Theory, Design and Applications*, 6th ed.; Butterworth-Heinemann: Oxford, UK, 2014; pp. 207–225.
6. Zhang, Z.; Wang, X.; Yan, Y. A review of the state-of-the-art in electronic cooling, e-Prime—Advances in Electrical Engineering. *Electron. Energy* **2021**, *1*, 100009. [[CrossRef](#)]
7. Yu, T.-P.; Lee, Y.-L.; Li, Y.-W.; Mao, S.-W. The Study of Cooling Mechanism Design for High-Power Communication Module with Experimental Verification. *Appl. Sci.* **2021**, *11*, 5188. [[CrossRef](#)]
8. Elnaggar, M.H.A.; Edwan, E. Heat Pipes for Computer Cooling Applications. In *Electronics Cooling*; Intech Open Science: London, UK, 2016; Chapter 4; pp. 52–73.
9. Smakulski, P.; Pietrowicz, S. A review of the capabilities of high heat flux removal by porous materials, microchannels and spray cooling techniques. *Appl. Therm. Eng.* **2016**, *104*, 636–646. [[CrossRef](#)]
10. Lee, J.H. Thermal Management Technology of TGP for High Heat-generation. *Korean Soc. Mech. Eng.* **2020**, *12*, 32–36.
11. Faghri, A. Review and Advances in Heat Pipe Science and Technology. *J. Heat Transf.* **2012**, *134*, 123001. [[CrossRef](#)]
12. Faghri, A.; Chen, M.; Morgan, M. Heat Transfer Characteristics in Two-Phase Closed Conventional and Concentric Annular Thermosyphons. *ASME J. Heat Transf.* **1989**, *111*, 611–618. [[CrossRef](#)]
13. Faghri, A.; Thomas, S. Performance Characteristics of a Concentric Annular Heat Pipe: Part I—Experimental Prediction and Analysis of the Capillary Limit. *J. Heat Transf.* **1989**, *111*, 844–850. [[CrossRef](#)]
14. Faghri, A.; Thomas, S. Performance Characteristics of a Concentric Annular Heat Pipe: Part II—Vapor Flow Analysis. *J. Heat Transf.* **1989**, *111*, 851–857. [[CrossRef](#)]
15. Boo, J.H.; Park, S.Y. An Experimental Study on the Thermal Performance of a Concentric Annular Heat Pipe. *J. Med. Sci. Technol.* **2005**, *19*, 1036–1043. [[CrossRef](#)]
16. Yan, X.K.; Duan, Y.N.; Ma, C.F.; Lv, Z.F. Construction of Sodium Heat-Pipe Furnaces and the Isothermal Characteristics of the Furnaces. *Int. J. Thermophys.* **2011**, *32*, 494–504. [[CrossRef](#)]
17. Choi, J.H.; Yuan, Y.; Borca-Tasciuc, D.A.; Kang, H.K. Design, construction, and performance testing of an isothermal naphthalene heat pipe furnace. *Rev. Sci. Instrum.* **2014**, *85*, 095105. [[CrossRef](#)] [[PubMed](#)]
18. Kammuang-lue, N.; Sakulchangsattajai, P.; Terdtoon, P. Effect of Working Orientations, Mass Flow Rates, and Flow Directions on Thermal Performance of Annular Thermosyphon. In Proceedings of the 8th International Conference on Mechanical and Aerospace Engineering 2017, Prague, Czech Republic, 22–25 July 2017; pp. 171–178.
19. Mustaffar, A.; Anh, N.P.; Reay, D.; Boodhoo, K. Concentric annular heat pipe characterization analysis for a drying application. *Appl. Therm. Eng.* **2019**, *149*, 275–286. [[CrossRef](#)]
20. Song, E.-H.; Lee, K.-B.; Rhi, S.-H.; Kim, K. Thermal and Flow Characteristics in a Concentric Annular Heat Pipe Heat Sink. *Energies* **2020**, *13*, 5282. [[CrossRef](#)]
21. Song, E.-H.; Lee, K.-B.; Rhi, S.-H. Thermal and Flow Simulation of Concentric Annular Heat Pipe with Symmetric or Asymmetric Condenser. *Energies* **2021**, *14*, 3333. [[CrossRef](#)]
22. Czajkowski, C.; Nowak, A.I.; Pietrowicz, S. Flower Shape Oscillating Heat Pipe—A novel type of oscillating heat pipe in a rotary system of coordinates—An experimental investigation. *Appl. Therm. Eng.* **2020**, *179*, 115702. [[CrossRef](#)]
23. Błasiak, P.; Opalski, M.; Parmar, P.; Czajkowski, C.; Pietrowicz, S. The Thermal—Flow Processes and Flow Pattern in a Pulsating Heat Pipe—Numerical Modelling and Experimental Validation. *Energies* **2021**, *14*, 5952. [[CrossRef](#)]
24. Khalili, M.; Shafii, M. Investigating thermal performance of a partly sintered-wick heat pipe filled with different working fluids. *Sci. Iran.* **2016**, *23*, 2616–2625. [[CrossRef](#)]

25. Alves, T.A.; Krambeck, L.; Santos, P.H.D. Heat Pipe and Thermosyphon for Thermal Management of Thermoelectric Cooling. In *Bringing Thermoelectricity into Reality*, 1st ed.; Aranguren, P., Ed.; Intech Open: London, UK, 2018; Chapter 17.
26. Kapekov, A. *Development of an Innovative Cooling Concept for Turbofan Engines*; KTH School of Industrial Engineering and Management: Stockholm, Sweden, 2018.
27. Liu, F.; Lan, F.; Chen, J. Dynamic thermal characteristics of heat pipe via segmented thermal resistance model for electric vehicle battery cooling. *J. Power Sources* **2016**, *321*, 57–70. [[CrossRef](#)]
28. Lee, Y.Y. An Investigation and Enhancement of Thermal Performance in a Heat Pipe and Its Thermal Modeling Application. Ph.D. Dissertation, Swinburne University of Technology, Kuching, Malaysia, 2018.
29. Shafieian, A.; Khiadani, M.; Nosrati, A. Theoretical modeling approaches of heat pipe solar collectors in solar systems: A comprehensive review. *Sol. Energy* **2019**, *193*, 227–243. [[CrossRef](#)]
30. Ciacci, C. 1D Modelling and Analysis of Thermal Conditioning Systems for Electric Vehicles. Ph.D. Dissertation, University of Windsor, Windsor, ON, Canada, 2019. Available online: <https://scholar.uwindsor.ca/etd/7779> (accessed on 19 January 2022).
31. Hu, G.; Hu, R.; Kelly, J.M.; Ortensi, J. *Multi-Physics Simulations of Heat Pipe Micro Reactor*; Report ID ANL-NSE-19/25; Argonne National Laboratory: Lemont, IL, USA, 2019.
32. Yoo, J.; Qin, S.; Song, M.; Hartvigsen, J.L.; Sellers, Z.D.; Morton, T.J.; Sabharwall, P.; Hansel, J.; Ibarra, L.; Feng, B.; et al. *Modeling and Analysis Support for High Temperature Single Heat Pipe Experiment: Current Status and Plan*; Report# INL/EXT-21-61961; Idaho National Laboratory: Idaho Falls, ID, USA, 2021.
33. Dong, Z.; Li, X.; Li, Z.; Hou, Y. Modeling Simulation and Temperature Control on Thermal Characteristics of Airborne Liquid Cooling System. *IEEE Access* **2020**, *8*, 113112–113120. [[CrossRef](#)]
34. Tao, X. Design, Modeling and Control of a Thermal Management System for Hybrid Electric Vehicles. Ph.D. Dissertation, Clemson University, Clemson, SC, USA, 2016.
35. Ayad, M.; Jubori, A.; Jawad, Q.A. Computational evaluation of thermal behavior of a wickless heat pipe under various conditions. *Case Stud. Therm. Eng.* **2020**, *22*, 100767. [[CrossRef](#)]
36. Adrian, Ł.; Szufa, S.; Piersa, P.; Mikołajczyk, F. Numerical Model of Heat Pipes as an Optimization Method of Heat Exchangers. *Energies* **2021**, *14*, 7647. [[CrossRef](#)]
37. Zhao, Z.; Zhang, Y.; Zhang, Y.; Zhou, Y.; Hu, H. Numerical Study on the Transient Thermal Performance of a Two-Phase Closed Thermosyphon. *Energies* **2018**, *11*, 1433. [[CrossRef](#)]
38. Girish, S.; Lavanya, K.; Krishna, P.G. CFD analysis of Pulsating heat pipe using different fluids. *Int. J. Mech. Eng. Technol. (IJMET)* **2017**, *8*, 804–812.
39. Kloczko, S. Experimental Investigation and Numerical Simulation of Loop Thermosyphons. Master's Thesis, University of Connecticut, Mansfield, CT, USA, 2019.
40. Rhi, S.H.; Lee, K.B.; Chae, H.I. 3-Dimensional Annular Heat Sink. Korea Patent No. 10-2019-0133835, 25 October 2019.
41. SIEMENS. *Integration Algorithms and Library User Guides Used in Simcenter Amesim*; SIEMENS: Munich, Germany, 2020.
42. Brennan, P.J.; Krocliczek, E.J. *Heat Pipe Design Handbook*; National Aeronautics and Space Administration: Washington, DA, USA, 1979.
43. Holman, J.P. *Heat Transfer*, 10th ed.; McGraw-Hill Book Company: New York, NY, USA, 2010.
44. Park, Y.Y.; Jeong, Y.S.; Bang, I.C. Design Study of Heat Pipes for Nuclear Spaceship Applications. In Proceedings of the Transactions of the Korean Nuclear Society Spring Meeting, Jeju, Korea, 23–24 May 2019.
45. National Instruments. Calculating Thermocouple Measurement Error in DMM/Switch Temperature Measurement Systems. In *Tutorial of National Instruments*; National Instruments: Austin, TX, USA, 2012.